Journal of Applied Fluid Mechanics, Vol. 18, No. 10, pp. 2627-2640, 2025.
Available online at www.jafmonline.net, ISSN 1735-3572, EISSN 1735-3645.
https://doi.org/10.47176/jafm.18.10.3426

Multi-objective Optimization of the Bionic Blade in the Multi-blade Centrifugal Fan for Electric Vehicles Application Based on an Orthogonal Test

J. Tang[1], J. Xu[2], B. Huang[1], J. Wang[2], L. Xu[2] and X. Chen[1†]

[1] *Zhejiang Key Laboratory of Multiflow and Fluid Machinery, Zhejiang Sci-Tech University, Hangzhou, Zhejiang, 310018, P. R. China*
[2] *Key Laboratory of Smart Thermal Management Science & Technology for Vehicles of Zhejiang Province, Zhejiang Yinlun Machinery Co., Ltd., Taizhou, P.R. China*

†*Corresponding Author Email: chenxp@zstu.edu.cn*

ABSTRACT

The multi-blade centrifugal fan, whose aeroacoustic properties significantly affect the noise, vibration and harshness performance of electric vehicles, is an important part of the automotive air conditioning system. A multi-blade centrifugal fan with a sawtooth trailing edge and a bionic blade is used. Multi-objective optimization of the bionic blade is investigated at the best efficiency point based on the orthogonal test to reduce sound pressure level (SPL) and ensure good aerodynamic performance. It is shown by the orthogonal test that the optimal combination of the three influencing factors is when the serration number, aspect ratio, and passivation ratio are 35, 1.5, and 0.2, respectively. The optimal model has 1.94% lower SPL than the original model, and the total pressure of both is basically unchanged. The presence of serration helps to mitigate vortex structures near the blade's trailing edge. The dominant frequency is not influenced by the bionic blade and matches the frequency of blade passage. The maximum SPL is approximately 1,250 Hz for both models, with a maximum deviation of approximately 2.1 dB. The frequency bandwidth of the main noise source is between 1,250 and 1,600 Hz, showing a considerable difference between the two models.

Article History

Received February 5, 2025
Revised May 7, 2025
Accepted May 20, 2025
Available online August 5, 2025

Keywords:

Multi-blade centrifugal fan
Bionic blade
Electric vehicles
Orthogonal test
Sound pressure level
Total pressure

1. INTRODUCTION

Multi-blade centrifugal fans, characterized by its compact size and high aerodynamic performance due to its dense blade configuration and numerous blades (Zhang et al., 2023), are widely employed in scenarios with limited space, such as automotive air conditioning systems, building ventilation, and heat exchange and cooling. In recent years, the technology of electric vehicles has developed rapidly, and its core performance indicators include noise, vibration, and vibration harshness (NVH) (Yang et al., 2015). The transmission components are mainly driven by the electric motor, rather than the engine as in traditional vehicles. After losing the cover of aerodynamic noise caused by the engine, the aerodynamic noise caused by the multi-blade centrifugal fan will be particularly prominent. Therefore, ways on how to reduce the aerodynamic noise of multi-blade centrifugal fan must be investigated to ensure good aerodynamic performance.

Numerous researches have examined aerodynamic performance (Yuan et al., 2023; Zhang et al., 2023; Chen et al., 2024) and aerodynamic noise (Paramasivam et al., 2017; Chen et al., 2018; Ottersten et al., 2021) of centrifugal fans. Changes in centrifugal fans construction can reduce aerodynamic noise and enhance performance. Paramasivam et al. (2015) examined the effects of a truncated guide vane on centrifugal fan tonal noise, discovering guide vanes can mitigate such noise. Azem et al. (2018) observed that pressure recovery units improve centrifugal fan efficiency, mainly because they can convert a large portion of kinetic energy into static pressure. Burgmann et al. (2018) identified that diffuser width modulation could boost multi-blade centrifugal fan effectiveness by 7.1% under partial load conditions. Xu et al. (2023) proposed a novel flap-angle adjustment method, which makes the internal flow more stable and improves the energy efficiency of coal power centrifugal fans. Li et al. (2011) examined how expanded impellers in the unchanging volute affect centrifugal fans.

Nomenclature

A	number of experiments
a	serration top width
a_0^2	sound velocity
b	serration bottom width
d	impeller diameter
C_S	Smagorinsky constant
f	frequency
F_i	quality Capability Item
G_k	turbulent energy
G_b	turbulent kinetic energy
$H(f)$	Heaviside function
h	serration height
k	number of factors
L	orthogonal table
L_S	mixed length of grid
m	number of levels
N	Serration number
n	impeller rotational speed
P_t	total pressure
P_{ij}	compressive stress tensor
$P^2(f)$	power spectral density
p	static pressure
p'	sound pressure
Q	flow rate
R	range
S_r	Strouhal number
S_{ij}	resolved-scale strain rate tensor
T_{ij}	Lighthill stress tensor
t	time
u_i	fluid velocity
u_n	fluid velocity component
V	calculate the volume of the unit
v	kinematic viscosity
v_n	source plane velocity component
W	relative velocity
Z	number of blades
Ω_Z	vorticity in the z direction
μ_t	turbulent viscosity
ρ	density
κ	von Kármán constant
Δt	time step
τ_{ij}	shear stress tensor
δ_{ij}	Kronecker tensor
$\delta(f)$	Dirac function

Abbreviations

BEP	Best Efficiency Point
BPF	Blade Passing Frequency
SPL	Sound Pressure Level

Subscripts

1	inner dimensions
2	outer dimensions
max	maximum
x, y, z	Cartesian coordinate component

The blades were optimized parametrically with an adjusted Hicks Henne function to enhance centrifugal fan aerodynamics (Zhou et al., 2021). Wang et al. (2020) presented an innovative sound-absorbing construction to minimize centrifugal fan aerodynamic noise.

Biomimetic technology is widely used in engineering applications, and it has also been introduced into the design and research of rotating machinery (Tian & Lyu, 2022; Ye et al., 2022; Zhou et al., 2022). In centrifugal fans, a series of biomimetic volute tongues (Wu et al., 2020; Wang et al., 2021a; Liu et al., 2023) and blades (Lei et al., 2023; Wang et al., 2023) have been designed from the inspiration of birds and fishes, including the serrated structure. Wang and Liu (2022) analyzed pressure fluctuations, turbulence intensity, and vorticity to explain the noise reduction process of trailing-edge serrations of varied forms. Wang et al. (2021b) found that the leading-edge serrations effectively suppressed flow separation, alleviated pressure gradients, reduced turbulence, and considerably lowered fan noise in the mid-to-low frequency range. Kim et al. (2019) designed the top of centrifugal fan blades to be serrated, achieving sound pressure level (SPL) reduction of 5.5 dB. Yang et al. (2024) observed that the serrated construction breaks up leading-edge vortices, reducing blade pressure pulsation and SPL by more than 1 dB. The above research indicate that trailing edge serrations effectively reduce broadband noise by disrupting periodic vortex shedding and breaking down large-scale vortices into finer turbulence. Therefore, the serrated trailing edge design was chosen for implementation in this study.

All the aforementioned studies were analyzed on the basis of the single factor effect. These studies have elucidated a good understanding on aerodynamic noise and aerodynamic performance. However, the effect of these factors is not isolated but tend to interfere with each other, even showing strong nonlinear characteristics. Such problems can be effectively avoided by multi-objective optimization methods, including orthogonal tests (Xia et al., 2016; Jiaqiang et al., 2018; Wu et al., 2018; Liu et al., 2020), response surface methods (Sun, 2011; Li et al., 2015; Zhang et al., 2017; Chai et al., 2020; He et al., 2023), and fractional order experiments (Weissman & Anderson, 2015; Politis et al., 2017). Chen et al. (2011) optimized the biomimetic fan's performance and SPL in multiple responses using the Taguchi mass loss function. Fan et al. (2020) conducted an orthogonal optimization design with multiple parameters and objectives for a mixed flow fan and discovered that the pressure increase and efficiency of an optimized fan improved by 50.15% and 11.71%, respectively. Liu et al. (2024) performed orthogonal optimization on a centrifugal fan's impeller and volute, resulting in static pressure gain and efficiency improvements of 1.8% and 5%, respectively. However, no definitive results have been reported on the multi-objective optimization for bionic blade in the centrifugal fan for electric vehicle application.

The current study's primary goal is to optimize the bionic blade in centrifugal fans for electric vehicle application based on an orthogonal test. Specifically, the trailing edge of the blade is bio-inspired and designed into a sawtooth structure. Structural parameters including sawtooth number, aspect ratio, and passivation ratio are

considered to be influencing factors. SPL and total pressure are selected as optimization targets. This study aims to reduce sound pressure levels while maintaining a constant total pressure. Optimization is performed at the best efficiency point (BEP), and the corresponding flow rate and rotational speed are 400 m^3/h and 3000 rpm, respectively.

The structure of this paper is as follows: Section 2 covers governing equations and numerical approaches. Section 3 introduces the computational meshes and experimental validation of original multi-blade centrifugal fan. Section 4 presents the orthogonal experimental design and result analysis of the bionic blade. A comparative analysis of the aerodynamic characteristics and aerodynamic noise between the optimal model and original model is presented in Section 5. Finally, Section 6 summarizes the findings.

2. GOVERNING EQUATIONS AND NUMERICAL METHODS

2.1 Computational Fluid Dynamics (CFD) Method

This study employs the incompressible Navier-Stokes equations. The continuity and momentum equations are typically written as (Ye et al., 2017):

$$\frac{\partial u_i}{\partial x_i} = 0 , \tag{1}$$

$$\frac{\partial u_i}{\partial t} + \frac{\partial u_i u_j}{\partial x_j} + \frac{1}{\rho}\frac{\partial p}{\partial x_i} = F_i + \frac{\partial \tau_{ij}}{\partial x_j} , \tag{2}$$

here, ρ denotes the density, p represents the pressure, u_i denotes the velocity vector, F_i signifies the volumetric force vector. The shear stress tensor τ_{ij} is given by:

$$\tau_{ij} = v\left(\frac{\partial u_i}{\partial x_j} + \frac{\partial u_j}{\partial x_i} - \frac{2}{3}\frac{\partial u_l}{\partial x_l}\delta_{ij}\right) \tag{3}$$

where v is kinematic viscosity, δ_{ij} is the Kronecker tensor.

The initial simulation of consistent turbulence is carried out using the $k-\varepsilon$ model. Following this, the steady-state outcomes serve as the starting point for the flow field, enabling the application of large eddy simulation grounded in the Smagorinsky–Lilly model to simulate the dynamic turbulence in centrifugal fans. This approach has been validated across multiple investigations focused on rotating machinery (Tian & Lyu, 2022).

The eddy–viscosity is modeled as

$$\mu_t = \rho L_S{}^2 \left|\overline{S}\right| , \tag{4}$$

where $\left|\overline{S}\right| = \sqrt{2\overline{S_{ij}}\,\overline{S_{ij}}}$, S_{ij} is the resolved-scale strain rate tensor. L_S is the mixing length for subgrid dimensions, as specified:

$$L_S = \min\left(\kappa d, C_S V^{1/3}\right) , \tag{5}$$

To minimize the impact of subgrid-scale stress diffusion, a lower value of the Smagorinsky constant is typically preferred in the majority of numerical fluid flow analyses (Ye et al., 2022).

2.2 Ffowcs-Williams and Hawkings equation

The noise produced by the turbulent airflow is forecasted using a blend of methods. This methodology ties together Large Eddy Simulation with the Ffowcs-Williams and Hawkings model. The Ffowcs-Williams and Hawkings model illustrating how noises are generated when an object travels through a medium, and it can forecast the acoustic output from an analogous sound source (Khelladi et al., 2008). The Ffowcs-Williams and Hawkings equation is written as follows:

$$\frac{1}{a_0^2}\cdot\frac{\partial^2 \rho'}{\partial t^2} - \nabla^2 p' = \frac{\partial}{\partial t}\left\{\left[\rho_0 v_n + \rho\left(u_n - v_n\right)\right]\delta\left(f\right)\right\}$$

$$-\frac{\partial}{\partial x_i}\left\{\left[P_{ij} n_j + \rho u_i\left(u_n - v_n\right)\right]\delta\left(f\right)\right\} + \frac{\partial^2}{\partial x_i x}\left(T_{ij} H\left(f\right)\right) . \tag{6}$$

The first term in Eq. (6) is the monopole source, caused by blade thickness change; the second is the dipole source, caused by contact stresses at the fluid-wall interface; and the third is the quadrupole source, caused by internal flow stresses, with quadrupole noise typically omitted in low Mach number flows (Mach < 0.3).

In Eq. (6), u_n represents the velocity component of the fluid, v_n represents velocity component of the source plane, a_0^2 represents sound velocity, p' represents sound pressure, $\delta(f)$ is the Dirac function, $H(f)$ represents the Heaviside function, and P_{ij} represents the compressive stress tensor. T_{ij} is typically written as:

$$T_{ij} = \rho u_i u_j + P_{ij} - a_0^2\left(\rho - \rho_0\right)\delta_{ij} , \tag{7}$$

where δ_{ij} is the Kronecker tensor.

2.3 Numerical Settings

All calculations were done with ANSYS FLUENT 18.0. We employed the finite volume technique to solve the equations and selected a pressure-driven solver to handle the solving process. For spatial discretization of the derivative terms, we utilized a second-order upwind scheme, and to couple pressure and velocity, the trusty SIMPLE algorithm was implemented. To guarantee the precision of our calculations, we implemented a second-order accurate high-resolution method.

The flow medium is air at 27 °C with uniform density. For the impeller zone, a rotating frame of reference is established, whereas a fixed frame is applied to the remaining components. Every wall within the flow domain is configured as a no-slip surface. At the inlet, mass flow rate is specified, while the outlet is defined by pressure-outlet conditions.

For the Large Eddy Simulation calculation, the time

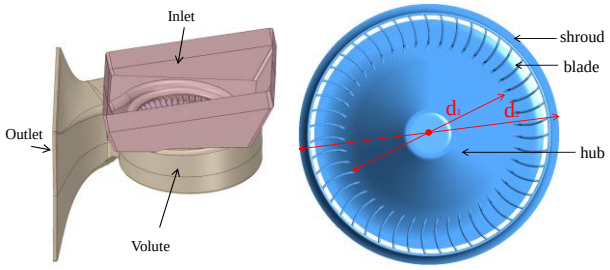

Fig. 1 Baseline model of the centrifugal fan (left) and impeller (right). d_1 and d_2 equals to 57mm and 80mm, respectively

Table 1 Impeller parameters of original multi-blade centrifugal fan

Parameters	Value
Impeller inner diameter d_1	57 mm
Impeller outer diameter d_2	80 mm
Blade thickness	1.38 mm
Impeller blade number Z	47
impeller speed n	3000 rpm

step is $\Delta t = 5.5556\times10^{-5} s$. The upper limit for iterations per time step is capped at 15. Flow fields evolved over 2,880 time steps, equating to eight impeller revolutions.

The Ffowcs-Williams model serves as the go-to framework for assessing noise in a centrifugal fan. The sound source surfaces are set on impeller. The sound is sampling period is set to 0.08 s.

3. COMPUTATIONAL MESHES AND EXPERIMENTAL VALIDATION OF ORIGINAL MODEL

3.1 Geometric Model

The base design of this study is a centrifugal fan for electric vehicles, as shown in Fig. 1. The fan has 47 blades. The impeller's inner and outer dimensions measure 57 mm and 80 mm, respectively. The fan speed is 3000 rpm and the flow rate is 400 m^3/h. Table 1 gives the specific parameters.

3.2 Computational Meshes

Fluent Meshing 18.0 segments the fluid field using polyhedral-shaped cells. The areas adjacent to the wall are encoded. To validate mesh convergence at Q_{BEP} (400 m^3/h), the rise in static pressure from inlet to outlet defines performance. The four mesh numbers are approximately 4.11 million, 4.93 million, 6.06 million, and 8.31 million. The correlation between static pressure and the grid count is presented in Fig. 2. The static pressure climbed 22.3 Pa with the mesh count rising from 4.11 to 6.06 million. At 8.31 million, the static pressure rise increases by just 2.3Pa compared to 6.06 million.

Thus, the mesh count of 6.06 million was selected. Out of this total, the rotating part consists of around 4.64 million elements, while the stationary section includes about 1.42 million elements, as detailed in Table 2. Figure 3 depicts the mesh pattern surrounding the centrifugal fan.

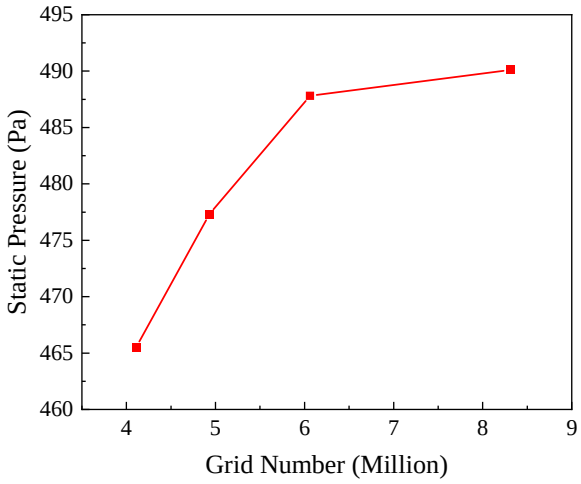

Fig. 2 Variation of static pressure with grid number at Q_{BEP}

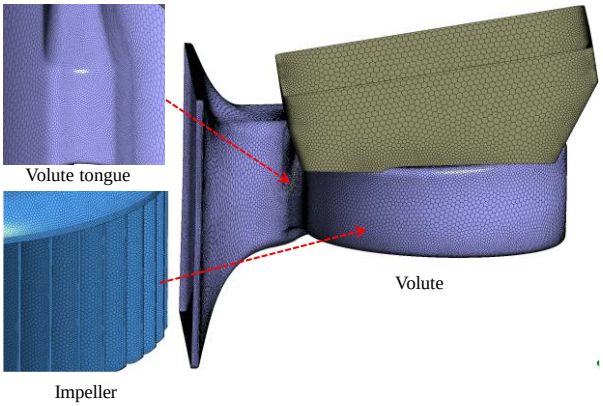

Fig. 3 Meshes around the original multi-blade centrifugal fan

Table 2 Number of grids in each computational domain

Computational domain	Number of grids (million)	average mesh size (mm)
Inlet domain	0.17	9.31
Outlet domain	0.30	9.31
Volute	0.95	1.41
Impeller	4.64	0.55
Total	6.06	0.91

3.3 Experimental Validation

Wind tunnel tests and semi-anechoic chamber measurements assessed the centrifugal fan's aerodynamic and noise profiles at Zhejiang Yinlun Machinery Co., Ltd.

Figure 4 illustrates the performance test system. Pressure sensors are installed at both the inlet and outlet of the primary chamber to track pressure differentials. Strategically placed flow nozzles at the chamber's midpoint control airflow velocity, allowing performance evaluation of the test fan under various operational conditions.

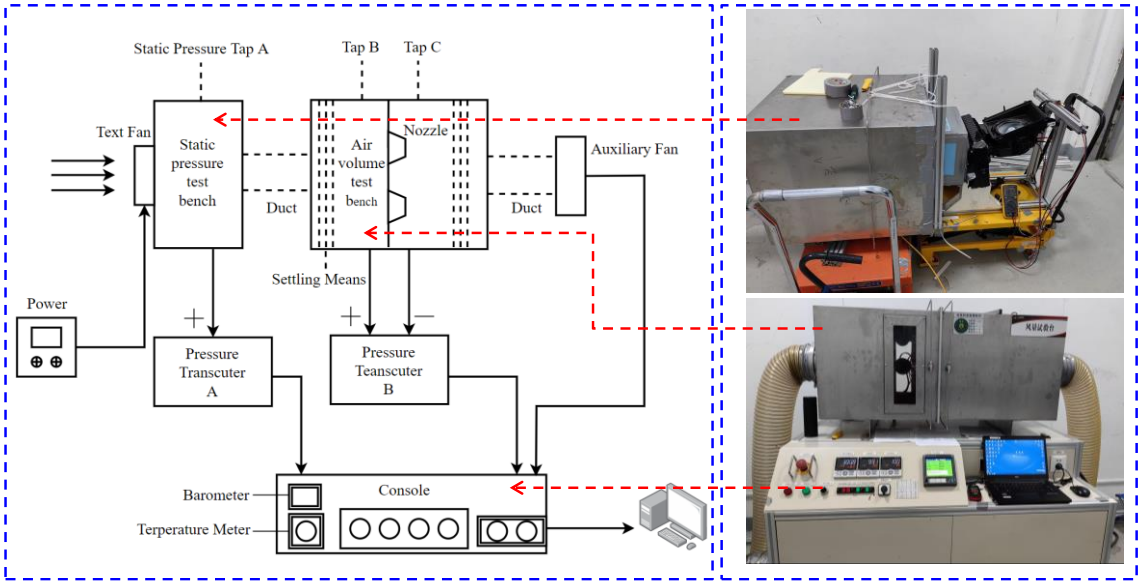

Fig. 4 Schematic of the aerodynamic experimental apparatus (left) and experimental apparatus (right)

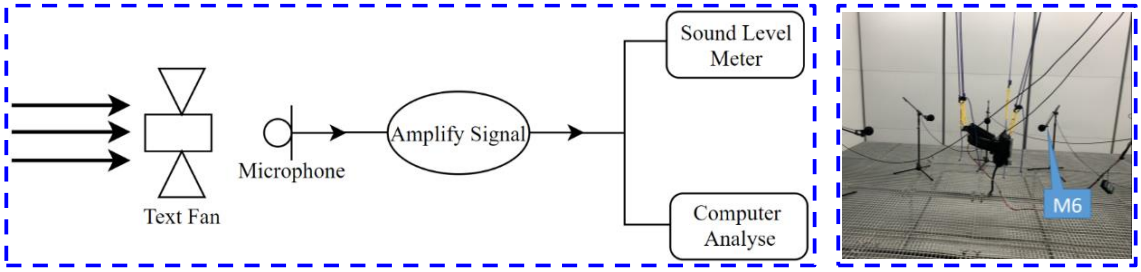

Fig. 5 Schematic of the aeroacoustic experimental apparatus (left) and the microphone positions in the semi-anechoic chamber (right)

Settling devices are placed both upstream and downstream of the primary enclosure to maintain uniform airflow distribution. Additionally, an extra cooling unit further regulates test fan performance.

Figure 5 shows the acoustic test system in the semi-anechoic room. This semi-anechoic room is capable of conducting noise tests with a constant air volume, with a background noise level of up to 16 dBA. The basic parameters of a semi-anechoic chamber are as follows: the deviation of the free sound field from 63 Hz to 630 Hz is less than ± 2.5 dB, the deviation of the free sound field from 600 Hz to 5,000 Hz is less than ± 2.0 dB, the deviation of the free sound field above 300 Hz is less than ± 3.0 dB, the room's cutoff frequency does not exceed 100 Hz, the radius of the free field is greater than 1.4 m, and the background noise (all indoor equipment is turned off) is ≤ 20 dB (A). The acoustic characteristics of the test fan is monitored by means of a microphone, which transforms incoming sound waves into electrical impulses. Then, the control system receives the electrical signal, analyzing it to determine the SPL. The acoustic receiver is designed in accordance with the GBT2888-2008 standard, and it's situated 1 meter from the test fan.

Figure 6 illustrates the correlation between static pressure and flow rates and compares these results with experimental data. Numerical simulation predicts static pressure trends matching experimental results across

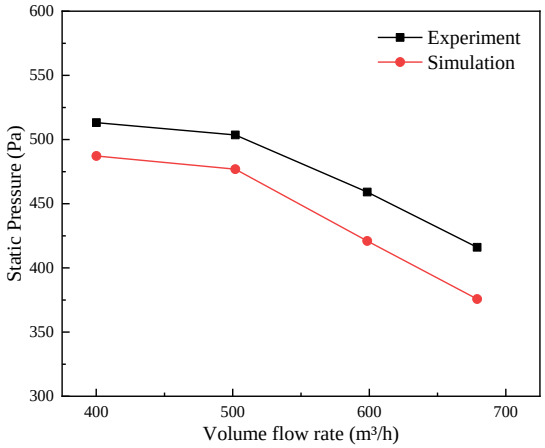

Fig. 6 Comparison of the external characteristic curves of the centrifugal fan

varying flow rates, but overall lower than the experimental results. The relative error of static pressure in this study within 10%, and its minimum value is 3.5%.

Figure 7 illustrates the correlation between SPL and flow rates and compares these results with experimental data. The deviation between the two methods is within 5.5% for all flow rates. The minimum relative error is approximately 1.9%, and its corresponding flow rate is 700 m³/h.

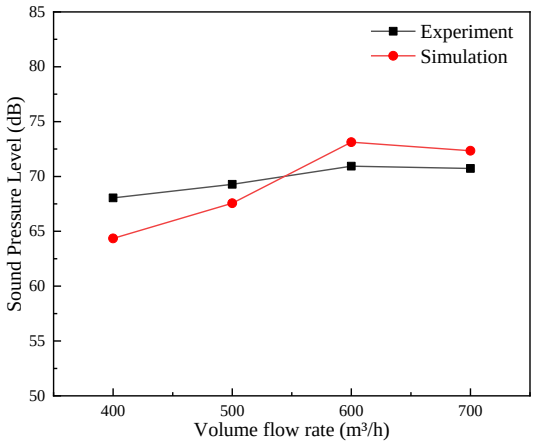

Fig. 7 Far-field noise comparison of centrifugal fans at different flow rates

The numerical and experimental results exhibit some divergence, potentially due to inherent inaccuracies in the simulation. However, the relative error in static pressure and SPL is within an acceptable range, making the numerical results reliable. Therefore, the numerical results can be considered reliable.

4. ORTHOGONAL TEST

4.1 Principle and Process of Orthogonal Test

The orthogonal test involves selecting representative combinations of factors and levels within a comprehensive test framework. This method analyzes the results of these selected combinations to reflect the overall tests situation and identify the optimal combination of factors. Orthogonal tests offer several advantages, including a reduced number of required tests, increased efficiency, and a simple test design.

The primary tool utilized in orthogonal tests is an orthogonal table, typically denoted by L. In an orthogonal table LA(m^k), "A" denotes the total number of experiments, "m" and "k" represent level count and factor quantity (Tan et al., 2023), respectively. When designing orthogonal table, an equal distribution of factor levels across each column and an equal occurrence of factor level combinations between any two columns must be ensured. The design and analysis of orthogonal test typically involve five main steps, as illustrated in Fig. 8.

Biomimetic blades are applied to the existing centrifugal fan. Inspired by the serrated trailing edge of owl wings (Fig. 9), the tailing edge of bionic blade is designed as a triangular serrated structure. The serrated region is located in the tailing edge leaf height of 6%–96%, with a total length of 45 mm. Three serrated structure parameters, namely, serration number (N), aspect ratio (h/b), and passivation ratio (a/b), are considered to reduce SPL and ensure good aerodynamic performance. The installation position and detailed structure of the serrations are shown in Fig. 10(b). In this study, each factor is investigated across five distinct levels. The serration number is varied at levels of 15, 20, 25, 30, and 35. The aspect ratio includes levels of 0.5, 1, 1.5, 2, and 2.5. The passivation ratio encompasses levels 0, 0.2, 0.4, 0.6, and 0.8, where 0 represents a serrated structure without passivation. The detailed factors and level parameters are provided in Table 3.

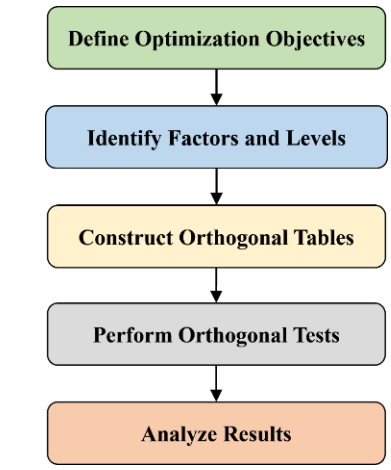

Fig. 8 Orthogonal test process

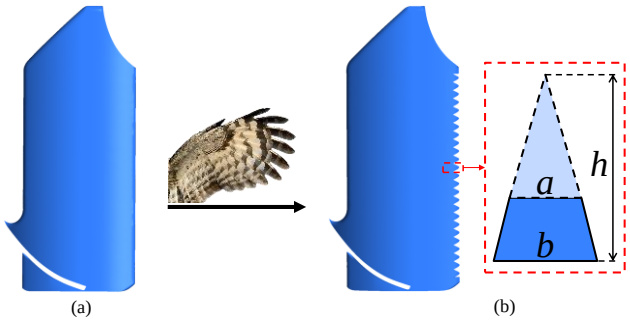

Fig. 9 Original blade model (a) and optimized blade model (b). The light-colored part is the passivation part

Table 3 Factors and levels of orthogonal test

Levels	Factors		
	Serration number (N)	Aspect ratio (h/b)	Passivation ratio (a/b)
1	15	0.5	0
2	20	1.0	0.2
3	25	1.5	0.4
4	30	2.0	0.6
5	35	2.5	0.8

4.2 Analysis of Orthogonal Test Results

This study adopted a three-factor five-level orthogonal test design; hence, the L25 (5^3) orthogonal table was selected, and a total of 25 tests were conducted. For the convenience of subsequent analysis, the serration number, aspect ratio, and passivation ratio are represented by A, B, and C, respectively.

Table 4 Factor level allocation scheme and test results of orthogonal test design

Tests	Code value			Real value			P_t	*SPL*
	A	B	C	A	B	C	(Pa)	(dB)
1	1	1	1	15	0.5	0	563.64	62.90
2	1	2	2	15	1.0	0.2	560.44	62.97
3	1	3	5	15	1.5	0.4	564.37	62.87
4	1	4	2	15	2.0	0.6	531.42	61.56
5	1	5	4	15	2.5	0.8	552.60	63.17
6	2	1	5	20	0.5	0.8	560.29	62.73
7	2	2	2	20	1.0	0.2	548.62	62.89
8	2	3	4	20	1.5	0.6	556.39	63.02
9	2	4	1	20	2.0	0	532.87	63.99
10	2	5	3	20	2.5	0.4	544.33	62.91
11	3	1	4	25	0.5	0.6	555.08	63.03
12	3	2	1	25	1.0	0	556.38	63.28
13	3	3	3	25	1.5	0.4	559.58	63.02
14	3	4	5	25	2.0	0.8	565.11	63.11
15	3	5	2	25	2.5	0.2	535.20	63.66
16	4	1	3	30	0.5	0.4	558.79	62.99
17	4	2	5	30	1.0	0.8	556.47	63.01
18	4	3	2	30	1.5	0.2	557.41	62.51
19	4	4	4	30	2.0	0.6	561.38	63.12
20	4	5	1	30	2.5	0	523.55	64.37
21	5	1	2	35	0.5	0.2	560.80	63.14
22	5	2	4	35	1.0	0.6	563.76	62.92
23	5	3	1	35	1.5	0	567.97	64.23
24	5	4	3	35	2.0	0.4	565.98	63.43
25	5	5	5	35	2.5	0.8	566.88	63.87

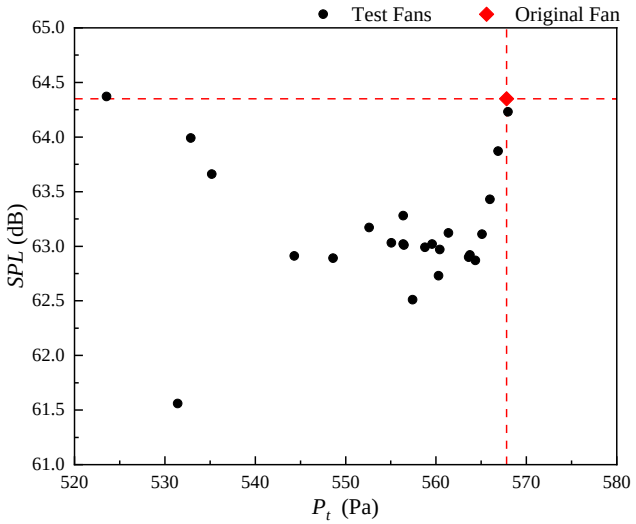

Fig. 10 Distributions of total pressure and SPL of test groups

Table 4 shows the scheme and results of the orthogonal test. Figure 10 illustrates the distribution of total pressure and SPL from 25 test groups and the original model. The original model has a total pressure of 567.8 Pa and an SPL of 64.35 dB. Table 4 and Fig. 10 reveal that with the exception of test group 23, the total pressure decreased across all test groups, suggesting that the trailing edge serration may reduce the centrifugal fan's total pressure. Regarding SPL, all models except for test group 20 exhibited decreased SPL, demonstrates that the serrated blade edge effectively lowers noise emissions from the centrifugal fan.

Table 5 Range analysis of mean total pressure (Unit: Pa)

Levels	A	B	C
1	554.49	559.72	548.88
2	548.50	557.13	546.69
3	554.27	**561.14**	557.82
4	551.52	551.35	557.84
5	**565.08**	544.51	**562.62**
R	16.58	16.63	15.93

Table 5 presents the mean total pressure range analysis. The table shows that the mean total pressure is between 544 and 566 Pa. The magnitude of this range reflects the varying impact of factors on total pressure, with larger ranges indicating greater impacts. According to Table 5, factor B (aspect ratio) has the most considerable effect on total pressure, followed by factor A (serration number), and lastly factor C (passivation ratio). By identifying the maximum mean total pressure, the optimal combination to increase total pressure is determined to be $A_5B_3C_5$.

Table 6 presents the range analysis of mean SPLs, indicating values ranging from 62 dB to 64 dB. A larger range, denoted as R, suggests a greater effect of factors on SPLs. According to Table 6, the most influential factor on SPLs is C (passivation ratio), followed by A (serration number), and finally B (aspect ratio). Additionally, the

Table 6 Range analysis of mean SPL (Unit: dB)

Levels	A	B	C
1	**62.69**	**62.96**	63.75
2	63.11	63.01	**62.75**
3	63.22	63.13	63.06
4	63.20	63.04	63.05
5	63.52	63.60	63.12
R	0.82	0.64	1.00

Table 7 Relative quantity R/R_{max} of each factor

	A	B	C
P_t	**0.99 (A_5)**	**1.00 (B_3)**	0.96 (C_5)
SPL	0.82 (A_1)	0.64 (B_1)	**1.00 (C_2)**

Table 8. SPL, total pressure and efficiency of optimal model

	SPL (dB)	P_t (Pa)	η (%)
Original model	64.35	564.80	57.88
Optimal model	63.10 (-1.94%)	566.63 (0.21%)	60.94 (5.29%)

optimal combination for reducing SPLs, identified on the basis of the minimum mean SPL, is $A_1B_1C_2$.

In view of centrifugal fans for electric vehicles, the peak total pressure is expected to increase, and the noise level will decrease. However, given the incomplete nature of orthogonal tests, achieving optimal results simultaneously is challenging. This study introduces the relative parameter R/R_{max} (Table 7) to resolve the issue. The optimal combination is $A_5B_3C_2$, corresponding to 35 serrations, an aspect ratio of 1.5, and a passivation ratio of 0.2. The relatively optimal combination $A_5B_3C_2$ is not found in the orthogonal table, and further modeling and numerical computations are required to ascertain its effectiveness in optimizing total pressure and SPL. Table 8 illustrates the optimal fan's total pressure at 566.63 Pa and its SPL at 63.10 dB. The total pressure remains largely stable, with the SPL decreasing by roughly 2% relative to the original fan's outcomes. Meanwhile, the efficiency of optimal model is improved by 5.29%.

5. COMPARISON AND ANALYSIS OF OPTIMAL MODEL AND ORIGINAL MODEL

5.1 Aerodynamic Characteristics

Figure 11 illustrates the streamline distributions at the impeller exit near the fan outlet (region A) and near the volute (region B) at the 1/4 blade height section. The blade serration can considerably reduce vortex formation.

The instantaneous vorticity distributions of the impeller fluid region at the 1/4 blade height section are shown in Fig. 13. Primary regions of high vorticity are located at the blade's leading and trailing edges, as well as near the pressure side of the channel. The optimal model exhibits weaker vorticity than the original. The vorticity distribution in the optimal model is more uniform, and the vorticity value is also lower, especially in the impeller

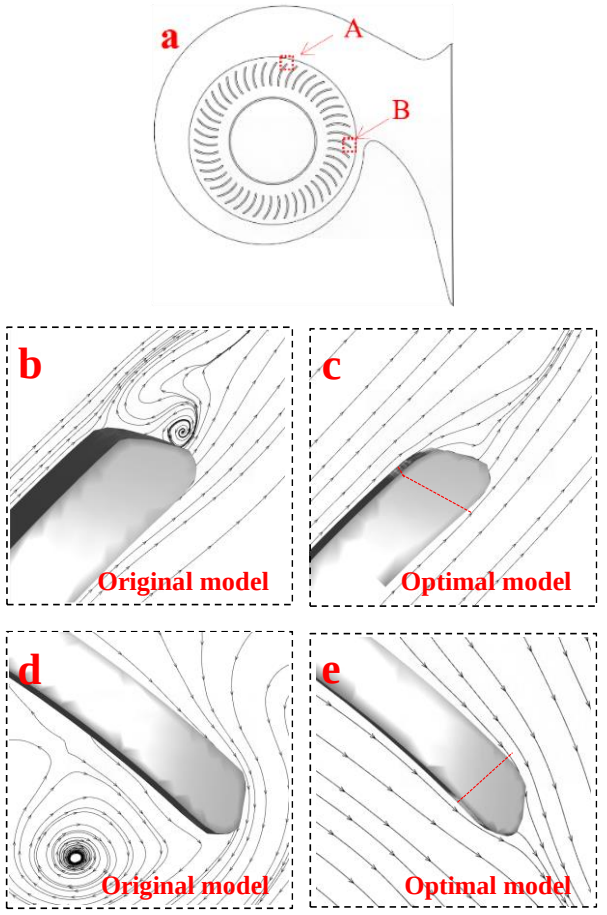

Fig. 11 Streamline distribution of blade trailing edge of the original and optimal models. (b) and (c) are region A; (d) and (e) are region B

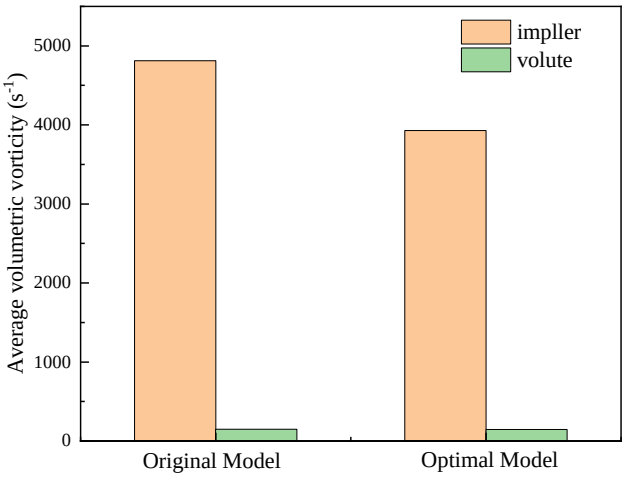

Fig. 12 Mean volumetric vorticity of the original and optimal models

outlet region (red dashed circle region), which considerably reduces the high vorticity region. This result indicates that the optimized model improves the flow state and reduces flow separation. The mean vorticity in the impeller fluid region is approximately 4800 s^{-1} for optimal model and 3900 s^{-1} for original model, as shown in Fig. 12. Meanwhile, the impeller domain exhibits significantly higher mean vorticity than the volute domain. The mean

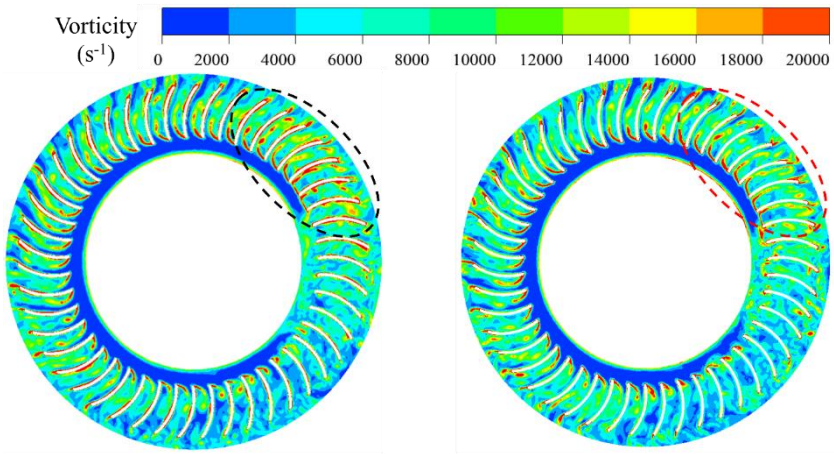

Fig. 13 Distributions of instantaneous vorticity in the impeller fluid region of original model (left) and optimal model (right)

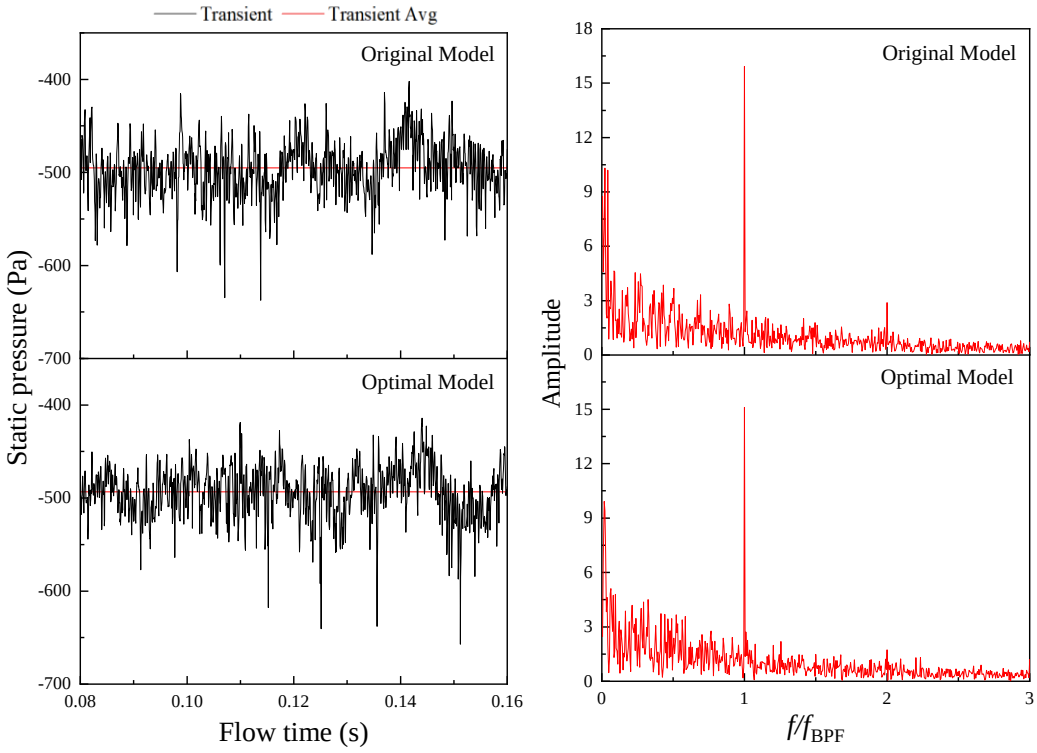

Fig. 14 Time domain diagram (left) and frequency domain diagram (right) of the pressure fluctuations at the 1/4 blade height section at monitoring point B1

vorticity in the volute fluid region is approximately 145 for the optimal model and 150 for the original model.

Figure 14 (left) displays the pressure variation timeline at monitoring point B1. In the original model, the static pressure ranges from −637.46 Pa to −402.18 Pa, resulting in an amplitude of 235.28 Pa. The optimal model exhibited reduced amplitude. The mean static pressure is −495.11 Pa for the optimal model and −493.20 Pa for the original model.

The pressure frequency spectrum is analyzed through Fast Fourier transformation, with results in Fig. 14 (right). The first-order dominant frequency equals to blade passage frequency (BPF, and current fan's f_{BPF} = 2,350 Hz) for both fan models, and the corresponding amplitude is approximately 15.93 (original) and 15.09 (optimal), respectively. At the same time, it is accompanied by numerous pressure signals of other frequencies. The amplitude of these signals is also suppressed on the optimized model, especially at twice BPF.

5.2 Aerodynamic Noise

Figure 15 shows the SPL in different directions. The high-value region is mainly distributed between 180° (M5) and 270° (M7). The orientation of which corresponds to the fan outlet close to the tongue. The optimal model's SPL is lower than the original model at these three monitoring points. The maximum value of such decrease is 1.25 dB, and the corresponding orientation is M6. In

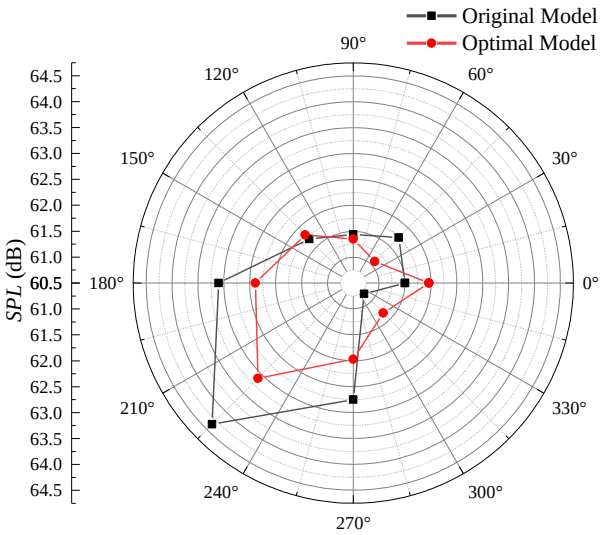

Fig. 15 Far-field noise directivity of the original and optimal models

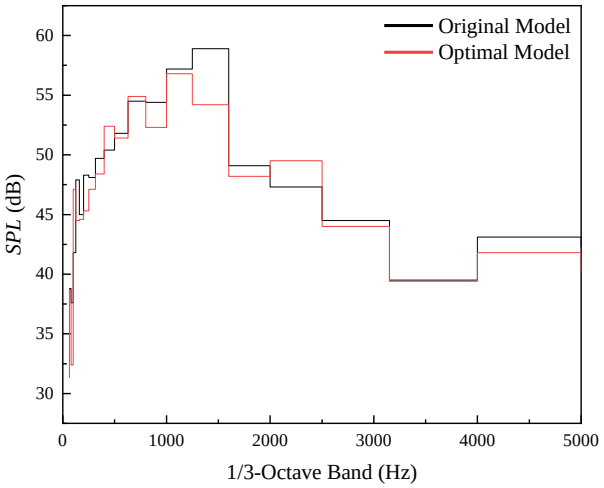

Fig. 16 1/3-octave spectra of SPL at M6 of the original and optimal models

addition, the difference of the SPL between the two models in other orientations is relatively small.

Figure 16 displays the 1/3 octave band SPL spectrum at monitoring point M6. The optimal model's SPL appears to be below the SPL achieved by the original model within the full frequency spectrum. The peak SPL occurs near 1,250Hz for both models. The maximum deviation is 2.1 dB.

Figure 17 shows the accumulative sound energy spectra for both models at monitoring point M6. The power spectral density of the received acoustic pressure was integrated to obtain an equation for the accumulative sound energy spectra. It was used to determine the acoustic energy contribution at each frequency (Liu et al., 2021). The equation is as follows:

$$E(f_i) = \int_o^{f_i} P^2(f)\,df\,, \tag{8}$$

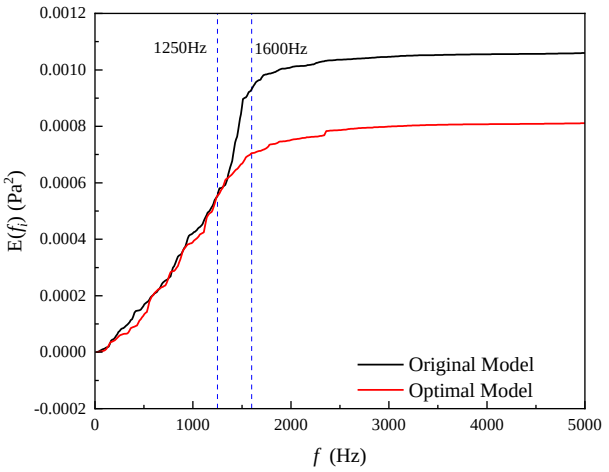

Fig. 17 Accumulated acoustic energy spectra at M6 of the original and optimal models

where $P^2(f)$ is the power spectral density. The slope of the spectrum is approximately 0.0006 Pa^2 for both models. This relationship is maintained until the frequency reaches 1,250 Hz. When the frequency is between 1,250 and 1,600 Hz, the accumulative sound energy spectrum obtained by the original model begins to be larger than that obtained by the optimal model. This difference increases sharply with increasing frequency. Afterward, the accumulative sound energy spectrum gradually becomes constant, and the values of the optimal and original models are 0.0008 and 0.001 Pa^2, respectively.

Figures 18 and 19 show the distributions of SPL on the impeller and volute noise sources between 1,250 and 1,600 Hz band range, respectively. The marked regions in Fig. 18, located at the tip and middle of the blade suction surface, exhibit a reduction in SPL in the optimized model. This improvement is attributed to the sawtooth structure, which effectively suppresses local noise by mitigating flow separation, thereby considerably reducing the high-noise regions. During impeller rotation, airflow impacts the volute wall and tongue, causing strong pressure fluctuations near the volute outlet. As shown in Fig. 19, the optimized model demonstrates lower SPLs at the volute tongue and volute surface compared with the original model.

6. CONCLUSION

Multi-blade centrifugal fans are an important part of air conditioning systems, whose aeroacoustics is crucial to the NVH performance of electric vehicles. Biomimetic blades are applied in the design of centrifugal fan, and then multi-objective optimization of the bionic structure is conducted to reduce noise and ensure good aerodynamic performance. The flow and sound fields are derived through numerical analysis, utilizing large eddy simulation flow analysis coupled with the Ffowcs-Williams and Hawkins acoustic model.

The original model is a multi-blade centrifugal fan without considering the bionic blade, whose flow rate and rotational speed at BEP are 400 m^3/h and 3,000 rpm. The accuracy of the simulations is validated through grid

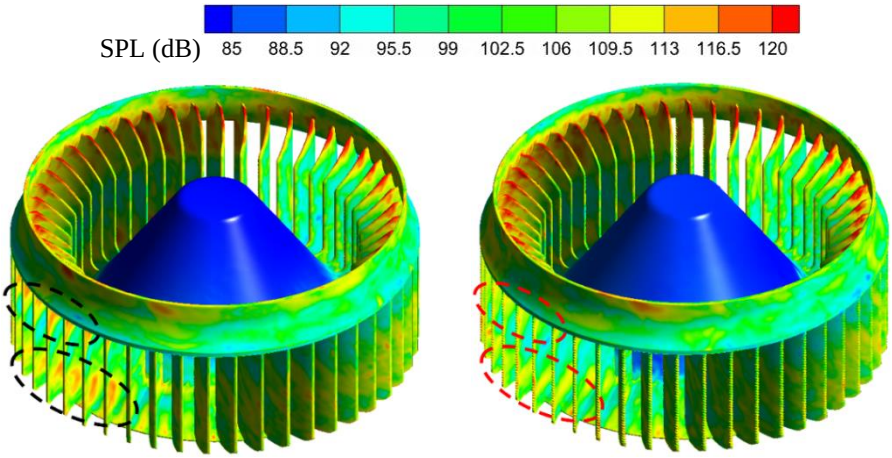

Fig. 18 SPL distributions of the impeller noise source between 1,250 Hz and 1,600 Hz band range (left) original model and (right) optimal model

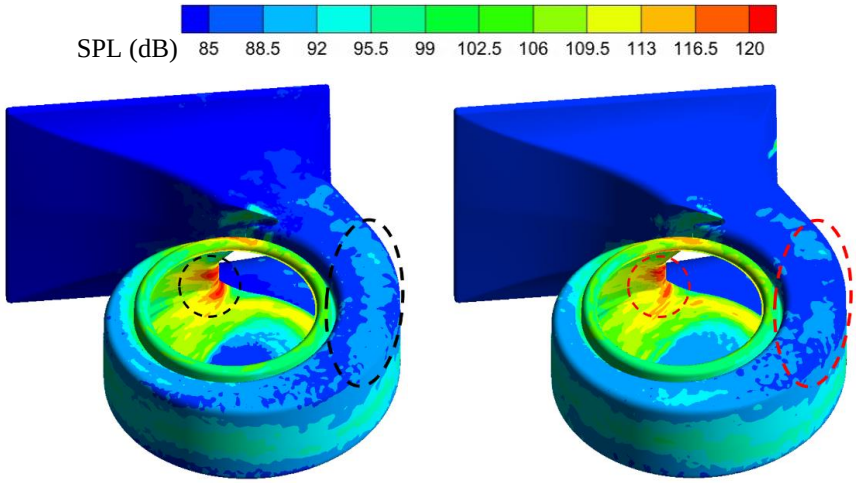

Fig. 19 SPL distributions of the volute noise source between 1,250Hz and 1,600 Hz band range (left) original model and (right) optimal model

independence tests and experimental data from Zhejiang Yinlun Machinery Co., Ltd.

Inspired by the wings of an owl, the tailing edge of the bionic blade in a centrifugal fan is designed as a serrated structure. During the orthogonal test of centrifugal fan at BEP, the influence factors include sawtooth number, aspect ratio, and passivation ratio, and SPL and total pressure are selected as optimization targets. The aspect ratio has the most considerable effect on fan total pressure, and fan noise is predominantly influenced by the passivation ratio. The optimized combination $A_5B_3C_2$ achieves a balance of increased total pressure and reduced SPL, that is, the serration number, aspect ratio, and passivation ratio are 35, 1.5, and 0.2, respectively. The total pressure remains largely the same as in the original model, and the SPL and efficiency of optimal model are respectively reduced and improved by approximately 1.94% and 5.29%.

A comparative analysis was conducted between the aerodynamic and acoustic characteristics of the optimal and original models. Trailing-edge serrations mitigate blade wake vortices. Moreover, the mean vorticity of the impeller fluid region for optimal model is 81.25% of that for original model. The first-order dominant frequency is insensitive to the serrated structure and equals to the blade passage frequency, whose optimal model exhibits reduced amplitude compared to the original. The peak SPL occurs near 1,250Hz for both models, and the maximum deviation is 2.1 dB. The accumulative sound energy spectrum shows that noise in the frequency band of 1,250–1,600 Hz is the main source of fan noise, whose slope decreases as the serrated structure is considered.

ACKNOWLEDGEMENTS

This work was financially supported by the Zhejiang Province Key R&D Project (Grant No. 2025C01044).

CONFLICT OF INTEREST

The authors assert no conflicts of interest, financial or personal, impacted this study.

AUTHORS CONTRIBUTION

Jibo Tang: Writing - Original Draft, Software, Visualization, Formal analysis. **Jinqiu Xu:** Resources, validation, Data curation. **Baoding Huang:** Writing - Review & Editing, Data curation, Software. **Jingxin Wang:** Resources, validation, Data curation. **Linjie Xu:** Resources, Investigation, validation. **Xiaoping Chen:** Methodology, Conceptualization, Writing - Review & Editing, Supervision.

REFERENCES

Azem, A., Mathis, P., Stute, F., Hoffmann, M., Müller, D., & Hetzel, G. (2018). Efficiency increase of free running centrifugal fans through a pressure regain unit used in an air handling unit. *Energy and Buildings*, *165*, 321–327. https://doi.org/10.1016/j.enbuild.2018.01.041

Burgmann, S., Fischer, T., Rudersdorf, M., Roos, A., Heinzel, A., & Seume, J. (2018). Development of a centrifugal fan with increased part-load efficiency for fuel cell applications. *Renewable Energy*, *116*, 815–826. https://doi.org/10.1016/j.renene.2017.09.075

Chai, X. Y., Xu, L. Z., Sun, Y. X., Liang, Z. W., Lu, E., & Li, Y. M. (2020). Development of a cleaning fan for a rice combine harvester using computational fluid dynamics and response surface methodology to optimise outlet airflow distribution. *Biosystems Engineering*, *192*, 232–244. https://doi.org/10.1016/j.biosystemseng.2019.12.016

Chen, J., He, Y., Gui, L., Wang, C. X., Chen, L., & Li, Y. R. (2018). Aerodynamic noise prediction of a centrifugal fan considering the volute effect using IBEM. *Applied Acoustics*, *132*, 182–190. https://doi.org/10.10 16/j.apacoust.2017.10.015

Chen, S. M., Wang, D. F., & Sun, S. M. (2011). Bionic fan optimization based on taguchi method. *Engineering Applications of Computational Fluid Mechanics*, *5*(3), 302–314. https://doi.org/10.1080/19942060.2011.11015373

Chen, Z. Y., He, H. J., Yang, H., Wei, Y. K., & Zhang, W. (2024). Asymmetric flow in a double-suction centrifugal fan induced by an inclined impeller. *Physics of Fluids*, *36*(1), 017113. https://doi.org/10.1063/5.0178927

Li, C. X., Wang, S. L., & Jia, Y. K. (2011). The performance of a centrifugal fan with enlarged impeller. *Energy Conversion and Management*, *52*(8–9), 2902–2910. https://doi.org/10.1016/j.enconman.2011.02.026

Jiaqiang E., Han, D. D., Qiu, A., Zhu, H., Deng, Y. W., Chen, J. W., Zhao, X. H., Zuo, W., Wang, H. C., Chen, J. M., & Peng, Q. G. (2018). Orthogonal experimental design of liquid-cooling structure on the cooling effect of a liquid-cooled battery thermal management system. *Applied Thermal Engineering*, *132*, 508–520. https://doi.org/10.1016/j.applthermaleng.2017.12.115

Fan, H. G., Zhang, J. S., Zhang, W., & Liu, B. (2020). Multiparameter and multiobjective optimization design based on orthogonal method for mixed flow fan. *Energies*, *13*(11), 2819. https://doi.org/10.3390/en13112819

He, S. H., Xiong, B. Y., Lei, H., Dong, K. J., Khan, S. A., & Zhao, J. Y. (2023). Optimization of low-temperature preheating strategy for Li-ion batteries with supercooling phase change materials using response surface method. *International Communications in Heat and Mass Transfer*, *142*, 106635. https://doi.org/10.1016/j.icheatmasstransfer.2023.106635

Khelladi, S., Kouidri, S., Bakir, F., & Rey, R. (2008). Predicting tonal noise from a high rotational speed centrifugal fan. *Journal of Sound and Vibration*, *313*(1–2), 113–133. https://doi.org/10.1016/j.jsv.2007.11.044

Kim, S. J., Sung, H. J., Wallin, S., & Johansson, A. V. (2019). Design of the centrifugal fan of a belt-driven starter generator with reduced flow noise. *International Journal of Heat and Fluid Flow*, *76*, 72–84. https://doi.org/10.1016/j.ijheatfluidflow.2019.01.016

Lei, J., Cui, Q., & Qin, G. L. (2023). Performance improvement and noise reduction analysis of multi-blade centrifugal fan imitating long-eared owl wing surface. *Physics of Fluids*, *35*(12), 125147. https://doi.org/10.1063/5.0184598

Li, D. Q., Jiang, S. H., Cao, Z. J., Zhou, W., Zhou, C. B., & Zhang, L. M. (2015). A multiple response-surface method for slope reliability analysis considering spatial variability of soil properties. *Engineering Geology*, *187*, 60–72. https://doi.org/10.1016/j.enggeo.2014.12.003

Liu, N. T., Jiang, C. Y., Huang, L. X., & Wang, C. (2021). Effect of porous casing on small axial-flow fan noise. *Applied Acoustics*, *175*, 107808. https://doi.org/10.1016/j.apacoust.2020.107808

Liu, Y., Li, Y., & Jiang, G. (2020). Orthogonal experiment on performance of mortar made with dune sand. *Construction and Building Materials*, *264*, 120254. https://doi.org/10.1016/j.conbuildmat.2020.120254

Liu, Y. H., Yuan, Q., Xu, Z. Q., Wu, L. M., & Liu, X. M. (2023). Bionic volute tongue optimization design of multi-blade centrifugal fan inspired by the wave leading-edge of humpback whale flippers. *Journal of Bionic Engineering*, *20*(5), 2209–2227. https://doi.org/10.1007/s42235-023-00354-w

Liu, Z. F., Wang, Z. D., Du, S. H., Yang, H., Wei, Y. K., & Zhang, W. (2024). Orthogonal optimization design of a Sirocco fan and numerical analysis on the internal flow characteristics. *Proceedings of the Institution of Mechanical Engineers, Part A: Journal of Power and*

Energy, *238*(1), 90–110. https://doi.org/10.1177/09576509231195120

Ottersten, M., Yao, H. D., & Davidson, L. (2021). Tonal noise of voluteless centrifugal fan generated by turbulence stemming from upstream inlet gap. *Physics of Fluids*, *33*(7), 075110. https://doi.org/10.1063/5.0055242

Paramasivam, K., Rajoo, S., & Romagnoli, A. (2015). Suppression of tonal noise in a centrifugal fan using guide vanes. *Journal of Sound and Vibration*, *357*, 95–106. https://doi.org/10.1016/j.jsv.2015.07.003

Paramasivam, K., Rajoo, S., Romagnoli, A., & Yahya, W. J. (2017). Tonal noise prediction in a small high speed centrifugal fan and experimental validation. *Applied Acoustics*, *125*, 59–70. https://doi.org/10.1016/j.apacoust.2017.04.009

Politis, S. N., Colombo, P., Colombo, G., & Rekkas, D. M. (2017). Design of experiments (DoE) in pharmaceutical development. *Drug Development and Industrial Pharmacy*, *43*(6), 889–901. https://doi.org/10.1080/03639045.2017.1291672

Sun, H. (2011). Wind turbine airfoil design using response surface method. *Journal of Mechanical Science and Technology*, *25*(5), 1335–1340. https://doi.org/10.1007/s12206-011-0310-6

Tan, D. L., Meng, Y. J., Tian, J., Zhang, C. T., Zhang, Z. Q., Yang, G. H., Cui, S. W., Hu, J. Y., & Zhao, Z. H. (2023). Utilization of renewable and sustainable diesel/methanol/n-butanol (DMB) blends for reducing the engine emissions in a diesel engine with different pre-injection strategies. *Energy*, *269*, 126785. https://doi.org/10.1016/j.energy.2023.126785

Tian, H. P., & Lyu, B. S. (2022). Prediction of broadband noise from rotating blade elements with serrated trailing edges. *Physics of Fluids*, *34*(8), 085109. https://doi.org/10.1063/5.0094423

Wang, C., Wang, M. Q., Mai, K., Li, H. Y., & Liu, N. T. (2020). Structure design of low-frequency broadband sound-absorbing volute for a multi-blade centrifugal fan. *Applied Acoustics*, *165*, 107315. https://doi.org/10.1016/j.apacoust.2020.107315

Wang, J. H., Liu, X. M., Tian, C. Y., & Xi, G. (2023). Aerodynamic performance improvement and noise control for the multi-blade centrifugal fan by using bio-inspired blades. *Energy*, *263*, 125829. https://doi.org/10.1016/j.energy.2022.125829

Wang, K., Ju, Y. P., & Zhang, C. H. (2021a). Aerodynamic optimization of forward-curved blade centrifugal fan characterized by inclining bionic volute tongue. *Structural and Multidisciplinary Optimization*, *63*(5), 2493–2507. https://doi.org/10.1007/s00158-020-02801-2

Wang, J. X., Ishibashi, K., Joto, M., Ikeda, T., Fujii, T., Nakata, T., & Liu, H. (2021b). Aeroacoustic characteristics of owl-inspired blade designs in a mixed flow fan: Effects of leading- and trailing-edge serrations. *Bioinspiration & Biomimetics*, *16*(6), 066003. https://doi.org/10.1088/1748-3190/ac1309

Wang, L., & Liu, X. M. (2022). Aeroacoustic investigation of asymmetric oblique trailing-edge serrations enlighted by owl wings. *Physics of Fluids*, *34*(1), 015113. https://doi.org/10.1063/5.0076272

Weissman, S. A., & Anderson, N. G. (2015). Design of Experiments (DoE) and process optimization. A review of recent publications. *Organic Process Research & Development*, *19*(11), 1605–1633. https://doi.org/10.1021/op500169m

Wu, L. M., Liu, X., & Wang, M. H. (2020). Effects of bionic volute tongue on aerodynamic performance and noise characteristics of centrifugal fan used in the air-conditioner. *Journal of Bionic Engineering*, *17*(4), 780–792. https://doi.org/10.1007/s42235-020-0067-7

Wu, Y. F., Zhao, H. X., Zhang, C. Q., Wang, L., & Han, J. T. (2018). Optimization analysis of structure parameters of steam ejector based on CFD and orthogonal test. *Energy*, *151*, 79–93. https://doi.org/10.1016/j.energy.2018.03.041

Xia, S. X., Lin, R., Cui, X., & Shan, J. (2016). The application of orthogonal test method in the parameters optimization of PEMFC under steady working condition. *International Journal of Hydrogen Energy*, *41*(26), 11380–11390. https://doi.org/10.1016/j.ijhydene.2016.04.140

Xu, W., Chen, G. L., Shi, H. J., Zhang, P. C., & Chen, X. M. (2023). Research on operational characteristics of coal power centrifugal fans at off-design working conditions based on flap-angle adjustment. *Energy*, *284*, 129363. https://doi.org/10.1016/j.energy.2023.129363

Yang, X. P., Yang, Y. R., Jiang, B. Y., Gao, X. Z., Hu, T. C., & Wang, J. (2024). Morphological effects of leading-edge sawtooth on the vortex evolution and acoustic characteristic of an ultra-thin centrifugal fan. *Physics of Fluids*, *36*(6), 065103. https://doi.org/10.1063/5.0206927

Yang, Z., Shang, F., Brown, I. P., & Krishnamurthy, M. (2015). Comparative study of interior permanent magnet, induction, and switched reluctance motor drives for EV and HEV applications. *IEEE Transactions on Transportation Electrification*, *1*(3), 245–254. https://doi.org/10.1109/TTE.2015.2470092

Ye, X. M., Zhang, J. K., & Li, C. X. (2017). Effect of blade tip pattern on performance of a twin-stage variable-pitch axial fan. *Energy*, *126*, 535–563. https://doi.org/10.1016/j.energy.2017.03.057

Ye, X. M., Zheng, N., Zhang, R. X., & Li, C. X. (2022). Effect of serrated trailing-edge blades on aerodynamic noise of an axial fan. *Journal of Mechanical Science and Technology*, *36*(6), 2937–2948. https://doi.org/10.1007/s12206-022-0526-7

Yuan, Y., Xiao, Y. H., Ming, P. J., & Lu, H. B. (2023). The aerodynamic and noise characteristics of centrifugal fan with partially tilted tongue. *Physics of*

Fluids, *35*(12), 127113. https://doi.org/10.1063/5.0176801

E. X. (2023). A design method of volute profile of multi-blade centrifugal fan based on DRBF model. *Physics of Fluids*, *35*(12), 125127. https://doi.org/10.1063/5.0180530

Zhang, L., Wu, K. X., & Liu, Y. (2017). Investigation on multi-objective performance optimization algorithm application of fan based on response surface method and entropy method. *Journal of Thermal Science*, *26*(6), 533–539. https://doi.org/10.1007/s11630-017-0970-3

Zhou, S. Q., Zhou, H. X., Yang, K., Dong, H. B., & Gao, Z. L. (2021). Research on blade design method of multi-blade centrifugal fan for building efficient ventilation based on Hicks-Henne function. *Sustainable Energy Technologies and Assessments*, *43*,100971. https://doi.org/10.1016/j.seta.2020.100971

Zhang, A. T., Zhou, B. S., Mao, C. Z., He, D. J., & Fang,

Zhou, T., Cao, H. J., Zhang, M. M., & Liao, C. C. (2022). Performance simulation of wind turbine with optimal designed trailing-edge serrations. *Energy*, *243*, 122998. https://doi.org/10.1016/j.energy.2021.122998